



The structure of the endoribonuclease XendoU: From small nucleolar RNA processing to severe acute respiratory syndrome coronavirus replication

Fabiana Renzi*, Elisa Caffarelli†, Pietro Laneve†‡, Irene Bozzoni†‡§, Maurizio Brunori*§¶, and Beatrice Vallone*

[†]Istituto di Biologia e Patologia Molecolari del Consiglio Nazionale delle Ricerche, [‡]Istituto Pasteur-Fondazione Cenci Bolognetti, [‡]Dipartimento di Genetica e Biologia Molecolare, and ^{*}Dipartimento di Scienze Biochimiche, University of Rome "La Sapienza," Piazzale A. Moro 5, 00185 Rome, Italy

Edited by Jennifer A. Doudna, University of California, Berkeley, CA, and approved June 26, 2006 (received for review March 24, 2006)

Small nucleolar RNAs (snoRNAs) play a key role in eukaryotic ribosome biogenesis. In most cases, snoRNAs are encoded in introns and are released through the splicing reaction. Some snoRNAs are, instead, produced by an alternative pathway consisting of endonucleolytic processing of pre-mRNA. XendoU, the endoribonuclease responsible for this activity, is a U-specific, metal-dependent enzyme that releases products with 2'-3' cyclic phosphate termini. XendoU is broadly conserved among eukaryotes, and it is a genetic marker of nidoviruses, including the severe acute respiratory syndrome coronavirus, where it is essential for replication and transcription. We have determined by crystallography the structure of XendoU that, by refined search methodologies, appears to display a unique fold. Based on sequence conservation, mutagenesis, and docking simulations, we have identified the active site. The conserved structural determinants of this site may provide a framework for attempting to design antiviral drugs to interfere with the infectious nidovirus life cycle.

crystallography | NendoU | protein structure | RNase family

Small nucleolar RNAs (snoRNAs), required for processing and modification of rRNA, are either independently transcribed or encoded in introns. The generation of most intron-encoded snoRNAs relies on the splicing reaction and leads to equimolar accumulation of spliced mRNA and snoRNA (1). Some snoRNAs are, instead, produced by a splicing-independent pathway: Endonucleolytic cleavages of the pre-mRNA release a pre-snoRNA that is converted to the mature form by exonucleolytic trimming (2, 3). In yeast, Rnt1p was shown to be the endonuclease responsible for the excision of intron-encoded snoRNAs and to be activated by the interaction with snoRNP factors assembled on the nascent transcript (3). Among higher eukaryotes, the endoribonuclease from *Xenopus laevis*, called XendoU, was shown to be responsible for processing the intron-encoded U16 and U86 snoRNAs (2, 4–6). XendoU cuts the RNA substrate at the level of short single-stranded uridine stretches. XendoU is unique among known endoribonucleases, because it generates products with 2'-3' cyclic phosphate and 5' OH termini and requires Mn²⁺ as an essential cofactor. XendoU is broadly conserved among metazoans (HomoloGene: 48394), even if the function of the homologous proteins is still hypothetical, as in the case of the human homolog (hpp11), described as a putative serine protease (7). Notably, a protein with sequence similarity to XendoU has been recently characterized in ssRNA(+) viruses of the Nidovirales order, including the coronavirus (CoV) responsible for the severe acute respiratory syndrome (SARS) (8). Studies aimed at characterizing the genome–proteome of SARS-CoV led to the isolation of a homolog of XendoU called NendoU. NendoU is a component of the replicase–transcriptase complex and exerts a critical role in virus replication and transcription (9). Interestingly, NendoU was found to cleave RNA at the level of uridines, releasing 2'-3' cyclic phosphate in the presence of Mn²⁺, although preferring

double-stranded RNA; however, as opposed to XendoU, the *in vivo* target of NendoU is still unidentified.

In this article, we report the three-dimensional structure of XendoU; extensive database searches failed to detect proteins with a similar fold; therefore, XendoU might belong to a previously unidentified superfamily. The description of the active site, identified by crystallography, mutagenesis, and phylogenetic data, allows us to define an evolutionarily conserved active-site architecture that seems to be flexibly used in different RNA-processing pathways.

Results and Discussion

Description of the Structure: A Unique Fold. We solved the structure of XendoU, a monomer of 292 residues, at 2.2-Å resolution by multiple isomorphous replacement (see Table 1). The asymmetric unit contains three monomers; residues 1–5, 45–53, and 290–292, being disordered, were not located in the map. The three-dimensional structure of XendoU is depicted in Fig. 1a, and a stereo projection is provided in Fig. 4, which is published as supporting information on the PNAS web site. Fig. 1 Upper reports the secondary structure distribution, and conveys relevant additional information concerning, among other things, residues that have been mutated. XendoU is a single-domain $\alpha+\beta$ protein with roughly globular shape (\approx 50-Å average diameter). It contains nine α -helices and three antiparallel β -sheets; the latter are clustered on one side of the protein (i.e., toward the observer in Fig. 1a) and account for 19% of the total amino acids, whereas the α -helices are largely on the other side and comprise \approx 34% of the residues. β -Sheets II and III are at an angle of \approx 30° to each other, creating a cavity; the strong curvature of β -sheet II interrupts the regularity of the H-bonds at the C terminus of β 3 and the N terminus of β 5 strands. Most connections between the β -strands are short hairpins, with the exception of a large loop joining β 3 and β 4. The α 7 helix, flanked by two loops, emerges in the cavity between β -sheets II and III.

The region encompassing the α 7 helix (amino acids 159–165) and the following loop (amino acids 166–179) contains several of the most conserved residues (see below), including some that are crucial for activity, as shown by mutagenesis (10). The buried side of the α 7 helix forms a hydrophobic cluster with residues from helices α 3, α 4, α 6, and α 9 and β -sheet III (Fig. 1 b and c), which contribute to locking its position and stabilizing its helical structure, given that its sequence displays β -strand propensity (11). The position of the loop 166–179 is stabilized by several

Conflict of interest statement: No conflicts declared.

This paper was submitted directly (Track II) to the PNAS office.

Abbreviations: CoV, coronavirus; SARS, severe acute respiratory syndrome; snoRNA, small nucleolar RNA; UMP, uridine monophosphate.

Data deposition: The atomic coordinates have been deposited in the Protein Data Bank, www.pdb.org (PDB ID code 2C1W).

*To whom correspondence should be addressed. E-mail: maurizio.brunori@uniroma1.it.

© 2006 by The National Academy of Sciences of the USA

Table 1. Crystal parameters, data collection, and refinement statistics for the native data collected at European Synchrotron Radiation Facility (ESRF) ID14eh1

Crystal parameters and data collection	
Cell dimensions (space group C2)	
a, Å	64.45
b, Å	53.20
c, Å	133.47
β, °	121.86
Solvent content, %	47.5
Resolution, Å	2.2
Total no. of observations	276,703
No. of unique observations	64,530
Mosaicity, °	1.1
Data completeness, %	96.0 (92.8)
$I/\sigma I$	8.8 (4.0)
Redundancy	4.3 (4.2)
R_{merge}^*	0.17 (0.39)
Data refinement	
Nonhydrogen atoms	
Protein (residues)	6,817 (823)
Water	438
PO_4^{2-} ligand	15
Resolution, Å	2.2
$R_{\text{factor}}^{\dagger}$	0.27
R_{free}	0.28
Rmsds from ideality	
Bond lengths, Å	0.015
Bond angles, °	1.788
Ramachandran plot	
Most favored, %	86.6
Allowed region, %	11.6
Generously allowed region, %	1.2
Disallowed, %	1.6

The values in parentheses are for the highest-resolution bin (approximate interval 0.15 Å).

* $R_{\text{merge}} = \sum((I_{hkl} - \langle I_{hkl} \rangle)^2) / \sum(I_{hkl}^2)$.

† $R_{\text{factor}} = \sum_{hkl} |F_o| - |F_c| / \sum_{hkl} |F_o|$ for all data except for 5%, which was used for free R calculation.

interactions. Residue E161 on $\alpha 7$ helix bridges the backbone of C158 and R170 by H-bonds; moreover, H-bonds between G166 and G176 (Fig. 1b) as well as between E167 and other residues in the loop (K169, Q172, E173, and M174) contribute to stabilizing its conformation. Notably, the mutation of residues E161Q/E167Q abolishes enzymatic activity (10), emphasizing that stabilization of this architecture is critical for catalysis. On the other side, the solvent-exposed surface of the $\alpha 7$ helix is surrounded by residues that are extensively conserved, i.e., H162 on $\alpha 7$ itself; T278 and Y280 on β -sheet III; and Y147, R149, G176, H178, and K224 on surrounding loops (Fig. 1b and c). Mutation of H162, H178, and K224 impairs catalysis in both XendoU (10) and NendoU (9).

We have carefully inspected (endo)ribonuclease families (12) to detect total or partial similarity with XendoU, especially at their active or binding site and searched for the motif defined by the $\alpha 7$ helix and its positioning with respect to β -sheets II and III. Because neither the main fold nor subdomains were identified in RNA-processing protein families, we carried out a search over the whole Protein Database (PDB) with DALI (13) and CE (14). Both programs yielded results below the significant threshold, identifying as structurally similar only a few noncontinuous secondary structure elements of <20 aa. Provisional classification was requested from the SCOP database (12) curator (A. Murzin, Medical Research Council Centre for Protein Engineering, Cambridge, U.K., personal communica-

tion) who confirmed that, given the absence of structures with relevant similarity, XendoU is, indeed, characterized by a unique fold.

A Previously Undescribed Structural Family of RNA-Processing Enzymes. We took advantage of structural information to expand phylogenetic analysis relative to previous results (8, 10). The alignment (Fig. 2), which extends from the $\alpha 6$ helix to the C terminus (residues 131–285) and includes XendoU homologs from a larger number of organisms, suggests that this region of the enzyme plays a critical functional role in these different organisms, given that many functionally important residues are conserved. Secondary structure prediction for the homologous proteins yields a pattern consistent with XendoU, suggesting that this region would adopt a consensus architecture.

The finding that homologs of XendoU are coded in a cyanobacterium (*Nostoc punctiforme*) and in at least one order of viruses is remarkable. Neither viruses nor bacteria are known to contain snoRNAs, and the bacterial enzymes that cleave and covalently modify the rRNA precursors are not ribonucleoproteins. Although possible, it seems to us quite unlikely that the function of these conserved proteins resembling XendoU is not RNA processing; after all, viral NendoU was, indeed, shown to process RNA *in vitro* (9). However, because NendoU was not detected in other RNA viruses, we assume that a horizontal gene transfer from a host cell to a nidoviral ancestor may have led to integration in the viral genome. On the other hand, the human homolog hpp11 (a tumor marker) has been attributed with a serine protease function (7). However, structural data cast some doubts on this assignment, because no canonical catalytic triad is found in homology modeling of hpp11 (45% sequence identity with XendoU); residues corresponding to H162, S157, and E161 (or D156) tend to cluster (Fig. 5, which is published as supporting information on the PNAS web site), but their relative orientation and distances deviate from the canonical triads. Moreover, experiments carried out to test whether XendoU is endowed with protease activity yielded negative results (data not shown).

Structure of the Phosphate-Binding Site. As shown in Fig. 1d, we detect a phosphate bound in between the $\alpha 7$ helix and the β -sheet III, at a short distance from some of the aforementioned conserved residues: H162 (2.7–3.7 Å), T278 (2.7–3.6 Å), H272 (2.0–2.8 Å), and N270 (3.2–4.5 Å) and one of the conformers of R149 (2.3–3.3 Å); values in parentheses indicate the range in distances observed among the three monomers in the asymmetric unit. This adduct is most likely due to the fact that crystallization was obtained in a concentrated phosphate buffer (0.2 M). Because we know that mutant H162A is inactive (10), we assume that residues interacting with the phosphate define the active site. In support of this assumption, we tested the role of T278 by producing and analyzing mutant T278A and found that the cleavage rate is reduced to 20% of the control (Fig. 3). This impaired activity is a specific local effect, because T278 makes no crucial interactions with the protein matrix and causes no misfolding or aggregation (as confirmed by CD and gel-filtration analysis).

In summary, the structure and mutagenesis allow us to conclude that the phosphate-binding site is crucial to the catalytic activity of XendoU. Interestingly, we notice that this site is reminiscent of the active site of both (i) RNaseT1 (15), where the phosphate of 3' GMP is held in place by H40, H92, Y38, and R77; and (ii) bovine RNaseA (16), where the phosphate of 3' CMP is surrounded by H119, H12, Q11, and K41. It seems that all these RNA-processing enzymes share some common residues in the active site (namely two His and one basic, either Arg or Lys).

Given the requirement for Mn^{2+} (or Mg^{2+}) in catalysis (5), we searched for a metal bound to XendoU, with negative results, even after 20 mM Mn^{2+} soaking of the crystals, or by absorption

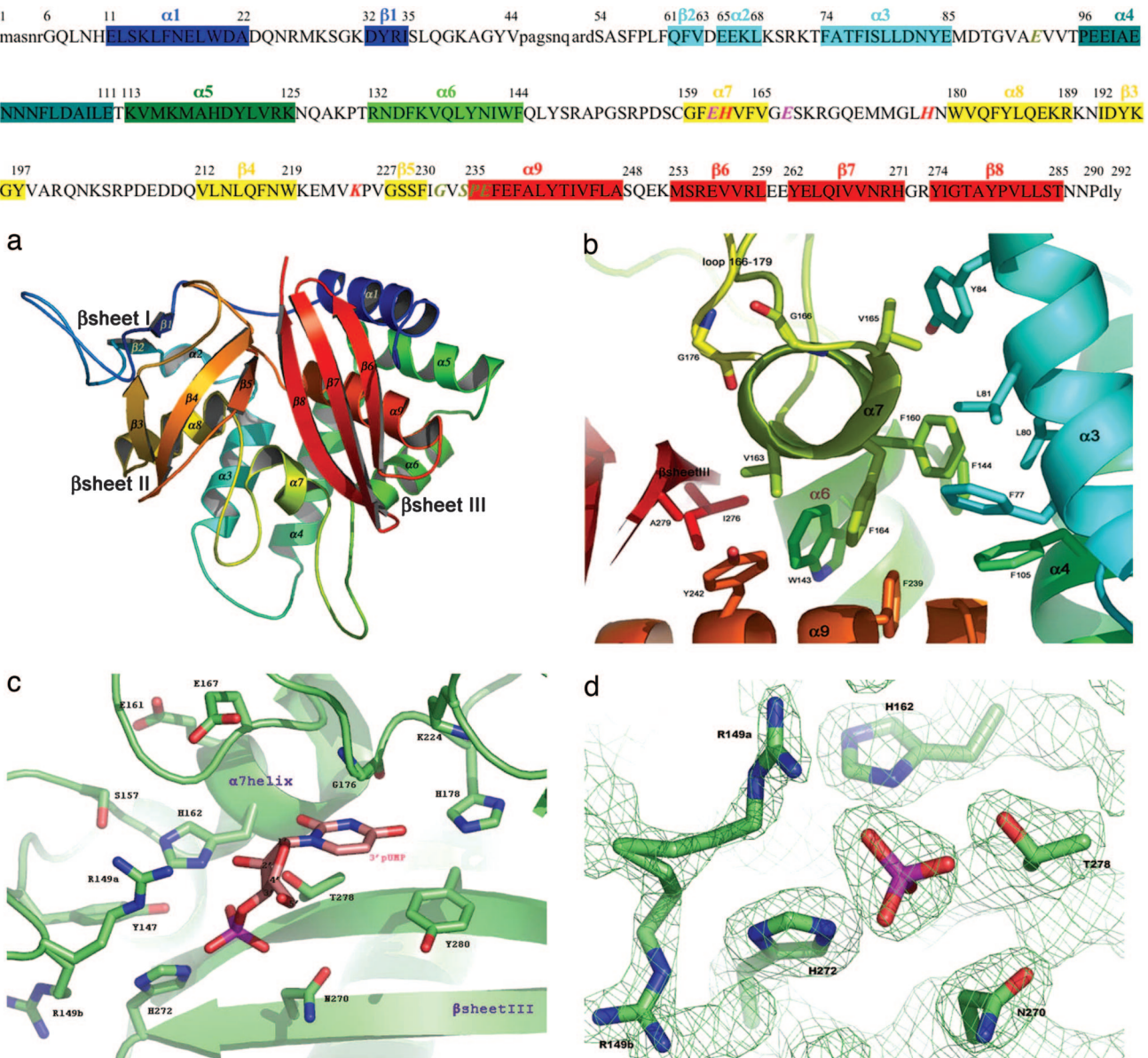


Fig. 1. The structure of XendoU. (Upper) Secondary structure of XendoU along the amino acid sequence. Secondary structure assignment is according to an algorithm implemented in PyMol. Colors change from blue to red going from the N to the C terminus. Residues not identified in the map are in lower case. Residues in italics have been mutated (12) as follows: dark yellow, nearly silent mutation; red, cleavage inactivation in single and double (E161Q + E167Q) mutants. T278 was mutated as described in Fig. 3. (Lower) (a) Cartoon representation of the overall fold of XendoU. The color code is as specified above. Helices are numbered from 1 to 9 and β-strands from 1 to 8. β-sheet I is formed by β1 and β2; β-sheet II by β3, β4, and β5; β-sheet III by β6, β7, and β8. (b) The α7 helix position is restrained. Conserved hydrophobic residues in the α7 helix form a hydrophobic cluster with residues belonging to α3, α4, α6, and α9 helices and β-sheet III. A H-bond between G166 and G176 (at the top) seals the ends of the loop 166–179. (c) Docking of the 3' UMP anchored onto the phosphate-binding site. The 3' UMP and the interacting residues are represented. In addition to the residues binding the phosphate, the conserved H178, Y280, and G176 (which appear to be in contact with the base) and S157 and Y147 (which may stabilize a proton on the Nε of H162) are shown. K224, E161, and E167 are also shown. (d) The 2Fo – Fc map contoured at 1.2σ on the phosphate-binding site. The phosphate is bound to residues H162, H272, N270, and T278 and to the positively charged R149 in one of its conformations.

spectroscopy (data not shown). This result casts some doubt on the hypothesis of a strong metal-binding site on the enzyme. It is possible that an efficient Mn²⁺ coordination may occur only in the ternary complex with RNA, as in RNaseP (17) and RNaseH (18).

Docking of Uridine Monophosphate (UMP) in the Structure. We attempted to gain structural insight into the complex of XendoU with its RNA substrate by soaking and crystallizing XendoU in the presence of a UMP nucleotide or with an oligoribonucleotide

(shown to be cut *in vitro*), in the presence of chelating agents to hinder cleavage; no ligand, however, was detected in the structure. Failure to obtain a complex may depend on low affinity for the oligoribonucleotide (as confirmed by repeated unsuccessful band-shift assays), suggesting the requirement for a full-length RNA precursor; in addition, the crystals were grown at high ionic strength, which may hinder the formation of a stable complex. Thus, we used the phosphate-binding site as the anchoring point for docking simulations of 3' UMP.

As shown in Fig. 1c, the nucleotide is predicted to be in contact

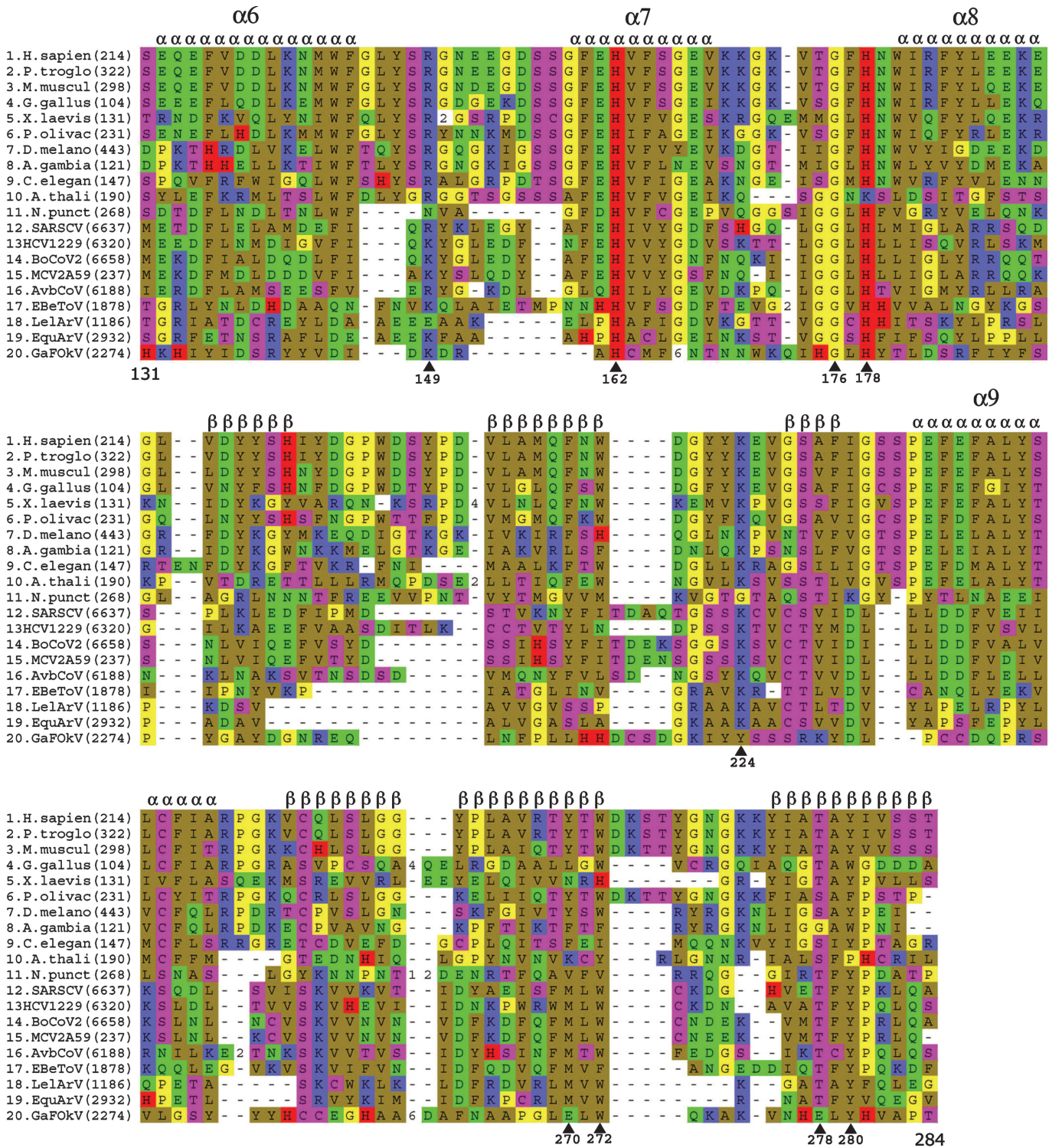


Fig. 2. Partial alignment of XendoU sequence (residues 131–285) with homologs from eukaryotes, nidoviruses, and a cyanobacterium. Alignment was performed by ClustalW (www.ebi.ac.uk/clustalw) and manually modified for consistency with the secondary structure prediction (29). Gaps were allowed in loops, and insertions are indicated by the total number of residues (to improve readability). Amino acid color codes are as follows: red, H; yellow, P/G; brown, hydrophobic; blue, R/K; green, D/E/N/Q; magenta, S/T/C. The top line indicates the secondary structure of XendoU. Residues forming the 3' UMP-binding site (described in Fig. 1d) are indicated by arrowheads. An abbreviated name of the organism and the number of the first amino acid of the aligned region are indicated. The corresponding data bank codes are as follows: Vertebrata: (1) *Homo sapiens* M32402, (2) *Pan troglodytes* XP_522366, (3) *Mus musculus* NP_032928, (4) *Gallus gallus* XM428848, (5) *Xenopus laevis* AJ507315, (6) *Paralichthys olivaceus* BAA88246; Insecta: (7) *Drosophila melanogaster* AAF47979, (8) *Anopheles gambiae* XP311978; Nematoda: (9) *Caenorhabditis elegans* NP_492590; Plantae: (10) *Arabidopsis thaliana* gi 25407557; Cyanobacteria: (11) *Nostoc punctiforme* NZ_AAAY02000132; Nidovirales-Coronaviridae: (12) SARS CoV NC_004718, (13) human CoV group 1 strain 229E NC_002645, (14) bovine CoV group2 NC003045, (15) murine hepatitis CoV strain A59 NC_001846, (16) avian infectious bronchitis CoV NC_001451, (17) equine Berne torovirus X52374; Nidovirales-Arteriviridae: (18) Lelystad arterivirus or porcine reproductive and respiratory syndrome virus M96262, (19) equine arteritis arterivirus X53459; Nidovirales-Roniviridae: (20) gill-associated factor okavirus AF227196.

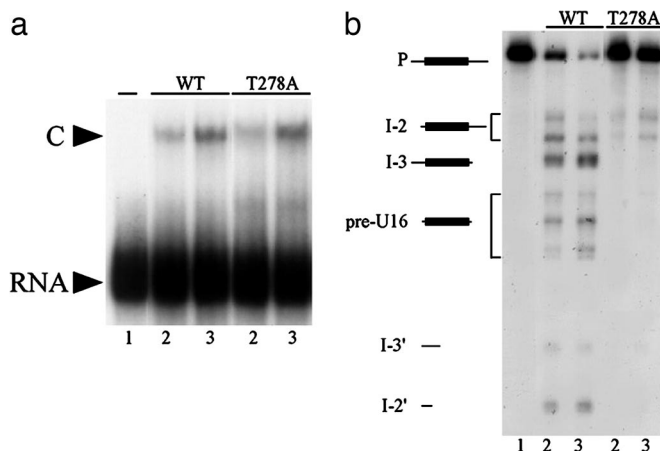


Fig. 3. Binding and processing activity of T278A mutant. (a) XendoU mutant can bind the RNA in a gel mobility-shift assay. Two femtomoles of ^{32}P -labeled U16 snoRNA precursor were incubated with His-XendoU or its mutant T278A at a concentration of $0.05 \mu\text{M}$ (lanes 2) or $0.1 \mu\text{M}$ (lanes 3); nonincubated RNA was loaded in lane 1 as control. C points to the RNA/protein complex. (b) *In vitro* processing assay. The ^{32}P -labeled U16 snoRNA precursor was incubated with 50 ng of His-XendoU (lanes WT) or T278A mutant (lanes T278A) for 10 min (lanes 2) or 20 min (lanes 3). As a control, nonincubated RNA was loaded in lane 1. The processing products are schematized at the left: The U16-containing precursor is indicated by P. Cleavage upstream to U16 produces the I-2 and the complementary cut-off molecule I-2', whereas cleavage downstream generates the I-3 and I-3' products. Double cleavage produces pre-U16 molecules. The intron is shown as a continuous line and the U16 snoRNA coding region as a black box.

with some of the most conserved residues. The base of UMP is accommodated in a crevice limited by the loop 166–176 and created by the presence, in position 176, of a Gly which is pulled back by the H-bond with the G166 (Fig. 1b). The O4 of UMP can form a H-bond (3.0 \AA) with H178, shown to be essential for cleavage (9, 10), whereas the pyrimidine ring may be engaged in a stacking interaction with the phenol ring of Y280. Docking simulations also provide a clue to speculation about a possible catalytic mechanism. At physiological pH, the N δ of H162 is likely to be deprotonated, because the proton on the N ϵ is stabilized by H-bonds to S157 or Y147 (see Fig. 1c). Being at H-bond distance from the 2' OH of the ribose, H162 may deprotonate the 2' OH of the ribose, making it available for a nucleophilic attack on the phosphorus, similarly to what is known for RNaseA (16). In addition, electrostatic interactions of the phosphate on the 3' side of UMP with R149 and K224 (whose mutation impairs catalysis) (9, 10) could stabilize the negatively charged pentacovalent intermediate; moreover, their interactions with the phosphate on the 5' side might contribute to enhancing substrate binding. The modeling cannot explain, however, the preference for a uridine substrate that might depend on structural constraints in the RNA substrate; U16 uridines cleaved *in vivo* are predicted to be in the loop of a stem-loop structure or to be preceded by a stem, as in the RNaseP substrate (19).

Concluding Remarks. XendoU is a member of a previously uncharacterized family of RNA processing enzymes, which recently raised considerable interest because of some homology with NendoU, an enzyme necessary for the maturation of the CoV responsible for SARS. Resolution of the three-dimensional structure of XendoU by crystallography represents a significant contribution to the description of an important pathway in RNA metabolism and allows us to identify a crucial architecture that is centered around α 7 helix (positioned in between β -sheets II and III) and the nearby loop comprising residues 166–178 (Fig.

1b and c). Analysis of the overall structure and extensive search in the PDB indicates that XendoU is a unique fold; in particular, comparison with other RNA processing enzymes supports this conclusion, indicating that XendoU may be taken as the prototype of a previously unknown family characterized by a peculiar active-site architecture. The crystallography reveals a phosphate bound by a number of amino acid side chains (Fig. 1d) that are reminiscent of those found in the active site of RNaseT1 and RNaseA. The crucial functional role of some of these active-site residues is confirmed by site-directed mutagenesis and activity assays. In addition, extensive phylogenetic analysis of homologs from eukaryotes, prokaryotes, and viruses proved (Fig. 2) that residues involved in the phosphate-binding site are highly conserved, providing evidence that this region is crucial to RNA processing. We believe that this consensus motif has been flexibly used in distinct RNA-processing pathways to fulfil specific needs of the different organisms, and we expect that characterization of the *in vivo* targets of viral and eukaryotic homologs might help to clarify this functional versatility. It is of great interest that mutation of some of these conserved residues abolishes the activity of NendoU, the homologous enzyme crucial to the maturation of the virus responsible for SARS (9). The description of the minimal structural determinants involved in nucleotide binding (as indicated by computer docking 3' UMP) (Fig. 1c) may represent a step toward the design of antiviral drugs that may selectively interfere with the life cycle of infectious nidoviruses.

Materials and Methods

Purification and Protease Assay. The ORF for the WT XendoU was cloned in the expression vector pQE30 (10) and expressed as N-terminal His₆-tagged protein in *Escherichia coli* M15 (pRep4). The N-terminal His₆-tagged protein was expressed in *E. coli* M15 (pRep4) and induced with 1 mM isopropyl β -D-thiogalactoside at 30°C for 4 h . Harvested cells were lysed in 50 mM phosphate buffer (pH 7.8) and 300 mM NaCl with 1 mg/ml lysozyme at 4°C for 2 h . After centrifugation, the filtered supernatant was applied to a NiNTA affinity column eluted in 150 mM imidazole; after dialysis against 10 mM Hepes (pH 7.8), 50 mM NaCl, and 20 mM EDTA, the protein was purified by HPLC gel filtration. Monomeric state and native folding were assessed by HPLC gel-filtration analysis and UVCD. For protease assay activity, 50 and 200 \mu M protein was incubated with 100 \mu M tosyl-Gly-Pro-Arg-pNO₂-anilide (a generic substrate for serine proteases) in 10 mM Hepes, 50 mM NaCl, and 20 mM EDTA, and absorbance was followed at 405 nm .

Crystallization and Data Collection. Crystals grew in a 1:1 mixture of protein (17 mg/ml) and reservoir solution (1.6 M ammonium sulfate and 0.2 M sodium phosphate, pH 5.5) at 20°C by hanging- and sitting-drop methods. Large nonsingle crystals were improved to platelets of maximum sizes $300 \times 300 \times 30 \text{ \mu m}$ by seeding techniques. Selenomethionine-labeled protein crystallized under the same conditions. X-ray data were collected at 100 K , and crystals were cryoprotected with 25% glycerol. Derivative data sets used in the multiple isomorphous replacement experiment were collected from (i) crystal soaked in 5 mM ethylmercuric-phosphate and 5 mM AuCN₄ for $\approx 1 \text{ h}$; (ii) crystals exposed to 20 atm ($1 \text{ atm} = 101.3 \text{ kPa}$) of xenon at 20°C for 5 min ; (iii) selenomethionine derivative crystals (for data statistics see Table 2, which is published as supporting information on the PNAS web site). Data were processed with Denzo/Scalepack and with Mosflm, as implemented in CCP4 (20–22). Crystals belonging to the monoclinic space group C2 contained three molecules in the asymmetric unit. They displayed heterogeneity in cell dimensions (see supporting information) and a solvent content ranging from 47.5% to 50% (22).

Structure Determination and Refinement. Substructure determination and refinement were performed with SOLVE-RESOLVE (23). Two multiple isomorphous replacement phasing sessions were carried out, using as native sets the form B crystals at 3.2-Å resolution or the Xe derivative at 2.55 Å (see supporting information). A partial model was manually built by COOT (24). Noncrystallographic symmetry (NCS) averaging was performed by using the DM-NCS program (22). The improved maps allowed to build most of the model whose geometries were then improved by simulated annealing in the program CNS (25). The refined model was then used to carry out molecular replacement with the nonisomorphous data set collected at 2.2-Å resolution by MolRep (22) (see Table 1). Each refinement cycle, carried out by using Refmac4 and Refmac5 (26), was alternated with a manual refitting using (2Fo – Fc) and (Fo – Fc) maps; R_{factor} and R_{free} values are 0.27 and 0.28, respectively.

The resulting model contains 819 of 876 amino acids (6–44 and 54–289 of the total 292 for each A, B, and C monomer), three phosphate ions, and 438 water molecules. Residues 1–5, 45–53, and 290–292 from all three monomers, residues 150–151 on monomer A, and 54–55 and 288–289 on monomer C were poorly defined in the map and were omitted.

Superposition of C α atoms from the A, B, and C monomers resulted in an average rmsd of 0.93 Å. PROCHECK (27) analysis calculated 98.4% of the protein in the allowed region of the Ramachandran plot. The 1.6% of residues in the disallowed region relate to the total of 739 nonproline, nonglycine residues for three monomers in the asymmetric unit and consist of 11 amino acids in seven sequence positions. These amino acids are located in external and relatively mobile segments that connect secondary structure elements.

Two amino acids (Gln-38 and Glu-261) are in not-allowed conformations in all three monomers and deserve particular attention. Gln-38 is in a very mobile long loop, which we could

not trace completely in the map, whereas Glu-261 is forced to adopt an unfavorable conformation to allow the tight chain inversion in the β -hairpin that connects β -strands 6 and 7.

3' UMP was docked manually by using COOT. Figures were produced by PyMol (28). Secondary structure predictions were carried out by PSIPRED (11).

Endonucleolytic Cleavage Assay for Mutant T278A. The construct expressing His-XendoU T278A was obtained by inverse PCR on pQE30-XendoU WT plasmid, with oligonucleotides T278Afw (GCCTACCCCGTCCTCCTGAGC) and T278Arev (GGC-CCCTATATAACGGCCGTGG). The mutant was expressed in M15 (pRep4) strain and purified by affinity chromatography. U16-containing precursor was transcribed *in vitro* in the presence of 20 μ Ci of [α -³²P]UTP (800 Ci/mmol) (1 Ci = 37 GBq) and 15 mM UTP. After transcription, the RNA was gel purified, phenol extracted, and precipitated with ethanol. For the binding assay, \approx 2 fmole of ³²P-labeled precursor were incubated with the WT or the mutant recombinant proteins, in the absence of Mn²⁺ (10); for the processing reaction, the same amount of RNA was incubated with proteins in the presence of 5 mM Mn²⁺ (5). The reaction products were analyzed on native or denaturing PAGE respectively, and visualized by autoradiography.

We thank A. Murzin for analyzing the XendoU coordinates before publication; A. Tramontano, G. Panetta, G. Sciaro, A. E. Miele, F. Altieri, and D. Tsernoglou for discussion; and M. Arceci for technical help. This work was supported, in part, by Ministero per l'Istruzione, Università e Ricerca of Italy Grants RBLA03B3KC-004, 2005050270_004, RBNE015MPB, and RBNE01KXC9 and the Centro di Eccellenza di Biologia e Medicina Molecolare (BEMM). Data were collected at the European Synchrotron Radiation Facility (ESRF) (Grenoble, France), the ELETTRA Synchrotron Light Laboratory (Trieste, Italy), and the Deutsches Elektronen-Synchrotron (DESY) (Hamburg, Germany).

1. Filipowicz, W. & Pogacic, V. (2002) *Curr. Opin. Cell. Biol.* **14**, 319–327.
2. Caffarelli, E., Arese, M., Santoro, B., Fragapane, P. & Bozzoni, I. (1994) *Mol. Cell. Biol.* **14**, 2966–2974.
3. Giorgi, C., Fatica, A., Nagel, R. & Bozzoni, I. (2001) *EMBO J.* **20**, 6856–6865.
4. Caffarelli, E., Fatica, A., Prislei, S., De Gregorio, E., Fragapane, P. & Bozzoni, I. (1996) *EMBO J.* **15**, 1121–1131.
5. Laneve, P., Altieri, F., Fiori, M. E., Scaloni, A., Bozzoni, I. & Caffarelli, E. (2003) *J. Biol. Chem.* **278**, 13026–13032.
6. Renzi, F., Filippini, D., Loreni, F., Bozzoni, I. & Caffarelli, E. (2002) *Biochim. Biophys. Acta* **1575**, 26–30.
7. Grundmann, U., Romisch, J., Siebold, B., Bohn, H. & Amann, E. (1990) *DNA Cell Biol.* **9**, 243–250.
8. Snijder, E. J., Bredenbeek, P. J., Dobbe, J. C., Thiel, V., Ziebuhr, J., Poon, L. M., Guan, Y., Rozanov, M., Spaan, W. J. M. & Gorbatenko, A. E. (2003) *J. Mol. Biol.* **331**, 991–1004.
9. Ivanov, K. A., Hertzig, T., Rozanov, M., Bayer, S., Thiel, V., Gorbatenko, A. E. & Ziebuhr, J. (2004) *Proc. Natl. Acad. Sci. USA* **101**, 12694–12699.
10. Gioia, U., Laneve, P., Dlakic, M., Arceci, M., Bozzoni I. & Caffarelli, E. (2005) *J. Biol. Chem.* **280**, 18996–19002.
11. McGuffin, L. J., Bryson, K. & Jones, D. T. (2000) *Bioinformatics* **16**, 404–405.
12. Murzin A. G., Brenner S. E., Hubbard T. & Chothia, C. (1995) *J. Mol. Biol.* **247**, 536–540.
13. Holm, L. & Sander, C. (1995) *Trends Biochem. Sci.* **20**, 478–480.
14. Shindyalov, I. N. & Bourne, P. E. (2001) *Nucleic Acids Res.* **29**, 228–229.
15. Zegers, I., Haikal, A. F., Palmer, R. & Wyns, L. (1994) *J. Biol. Chem.* **269**, 127–133.
16. Zegers, I., Maes, D., Dao-Thi, M., Poortmans, F., Palmer, R. & Wyns, L. (1994) *Protein Sci.* **3**, 2322–2339.
17. Kurz, J. C. & Fierke, C. A. (2002) *Biochemistry* **41**, 9545–9558.
18. Nowotny, M., Gaidamakov, S. A., Crouch, R. J. & Yang, W. (2005) *Cell* **121**, 1005–1016.
19. Loria, A. & Pan, T. (1997) *Biochemistry* **36**, 6317–6325.
20. Otwowski, Z. & Minor, W. (1997) *Methods Enzymol.* **276**, 307–326.
21. Leslie, A. G. W. (1992) *Joint CCP4/ESF EAMCB Newsletter on Protein Crystallography*, no. 26.
22. Collaborative Computational Project, Number 4. (1994) *Acta Crystallogr. D* **50**, 760–763.
23. Terwilliger, T. C. (2003) *Methods Enzymol.* **374**, 22–37.
24. Emsley, P. & Cowtan, K. (2004) *Acta Crystallogr. D* **60**, 2126–2132.
25. Brunger, A. T., Adams, P. D., Clore, G. M., DeLano, W. L., Gros, P., Grosse-Kunstleve, R. W., Jiang, J. S., Kuszewski, J., Nilges, M., Pannu, N. S., et al. (1998) *Acta Crystallogr. D* **54**, 905–921.
26. Murshudov, G. N., Vagin, A. A. & Dodson, E. J. (1997) *Acta Crystallogr. D* **53**, 240–255.
27. Laskowski, R. A., MacArthur, M. W., Mos, D. S. & Thornton, J. M. (1993) *J. Appl. Crystallogr.* **26**, 283–291.
28. DeLano, W. L. (2004) *The PyMOL Molecular Graphics System* (DeLano Scientific, San Carlos, CA). Available at www.pymol.org.